Brain Stimulation 18 (2025) 215–224

Contents lists available at ScienceDirect

Brain Stimulation

journal homepage: www.journals.elsevier.com/brain-stimulation

Locating activation sites of TMS with opposite current directions using probabilistic modelling and biophysical axon models

Ilkka Laakso [a,b,*], Juhani Kataja [a], Noora Matilainen [a], Timo Roine [c], Thomas Tarnaud [d], Yoshikazu Ugawa [e]

[a] Department of Electrical Engineering and Automation, Aalto University, Espoo, Finland
[b] Aalto Neuroimaging, Aalto University, Espoo, Finland
[c] Department of Neuroscience and Biomedical Engineering, Aalto University, Espoo, Finland
[d] Ghent University/IMEC, Ghent, Belgium
[e] Department of Human Neurophysiology, Institute of Brain Medical Sciences, Fukushima Medical University, Fukushima, Japan

ARTICLE INFO

Keywords:
Transcranial magnetic stimulation
Primary motor cortex
Computational modelling
Motor-evoked potential
Active motor threshold
Latency

ABSTRACT

Background: Motor responses evoked by transcranial magnetic stimulation (TMS) using posterior–anterior (PA) and anterior–posterior (AP) current directions have distinct latencies and thresholds. However, the underlying reasons for these differences remain unclear.
Objective: To quantify the differences in activation sites between PA- and AP-TMS.
Methods: Motor evoked potentials (MEPs) were recorded from five hand and arm muscles in nine healthy participants using both PA- and AP-TMS. Active motor thresholds were determined at 11 magnetic coil positions on the scalp. Probabilistic modelling was used to combine the measured threshold data with calculated electric field data from individual MRI-based models. This approach constructed 70 probability distributions of the activation site, dependent on the muscle and TMS direction.
Results: Modelling indicated that both PA- and AP-TMS more likely activated structures in white matter than in grey matter. PA-TMS activation sites were primarily in the white or grey matter in the precentral gyrus, while the AP-TMS activations were deeper and more posterior and lateral, likely within white matter under the postcentral and/or precentral gyri. Tractography and biophysical axon models provided a potential explanation on the location of activation sites: AP-TMS may activate the bends of white matter axons farther from M1 than PA-TMS, such that the conduction velocity along the neural tract could potentially explain the longer MEP latency of AP-TMS. The differences in activation sites among the five hand and arm muscles were small.
Conclusion: While a direct experimental confirmation of the activation sites is still needed, the results suggest that electric field analysis combined with tractography and biophysical axon modelling could be a useful computational tool for analysing and optimizing TMS.

Introduction

Transcranial magnetic stimulation (TMS) effects on the primary motor cortex depend on the orientation of the stimulation coil. Early TMS studies observed that reversing the current direction alters the responses when using monophasic current pulses [1]. Pulses delivered in the anteroposterior (AP) direction have longer latencies and higher motor thresholds compared to those delivered in the posteroanterior (PA) direction [1,2].

The differences between PA- and AP-TMS have been explained by the D- and I-wave hypothesis. D-waves are short-latency direct waves, followed by multiple periodic indirect (I) waves, measured in the corticospinal tract of cats and monkeys with direct cortical stimulation [3]. In humans, waves thought to be analogous to D- and I-waves have been observed from electrodes implanted in the epidural space during non-invasive electrical or magnetic stimulation [4]. At low intensities, TMS is thought to induce I-waves, which presumably originate from the activation of pyramidal tract neurones (PTNs) via presynaptic axons, as opposed to D-waves, which are likely due to direct activation of PTN axons [5]. The latency differences between PA- and AP-TMS measured with single motor unit electromyography (EMG) correspond to differences between I-waves, with the hypothesis that PA-TMS preferentially produces shorter latency I1-waves whereas

* Correspondence to: Aalto University, Otakaari 3, 02150 Espoo, Finland.
E-mail address: ilkka.laakso@aalto.fi (I. Laakso).

https://doi.org/10.1016/j.brs.2025.02.003
Received 15 July 2024; Received in revised form 22 November 2024; Accepted 5 February 2025
Available online 13 February 2025

AP-TMS produces later I3-waves [1,2].

TMS activates axons [6], as demonstrated by neural time constant measurements [7]. It has been hypothesized that these axons are activated either in the grey matter or in the bends just underneath the cortex [6]. However, the exact location of the activated axons and the reasons for the differences between PA- and AP-TMS remain unclear. Previous experimental–computational TMS localization studies have focussed on grey matter [8–11], assuming activation occurs there.

In this study, we investigate the differences between AP- and PA-TMS using a recently developed Bayesian modelling approach [12]. This method uses MRI-based models and measured motor threshold data to construct probability distributions of the activation site in the brain. Unlike previous modelling studies, we specifically examined the directional effects of TMS and did not limit our investigation into grey matter or the precentral gyrus. Our objectives are to determine the locations activated by PA- and AP-TMS, identify the activation sites of different muscles, and explain potential differences in the activation sites.

Methods

Participants

The data was collected from nine healthy right-handed participants (4 female, 5 male, mean age 30 ± 4.2, age range: 26–40). All participants gave their written consent for participation. The study was approved by the Aalto University Research Ethics Committee (decisions D/574/03.04/2022 and D/1006/03.04/2022). All procedures were conducted in accordance with the Declaration of Helsinki.

Magnetic resonance imaging and image processing

T1-, T2-, and diffusion-weighted MR images were acquired with a 3 T MRI scanner (Magnetom Skyra; Siemens Ltd., Erlangen, Germany). The parameters were as follows. T1-weighted: TR/TE/TI/FA/FOV/voxel size/number of slices = 1800 ms/1.99 ms/800 ms/9°/256 mm × 256 mm/1 mm × 1 mm × 1 mm/176; T2-weighted: TR/TE/FOV/voxel size/number of slices = 3200 ms/412 ms/256 mm × 256 mm/1 mm × 1 mm × 1 mm /176; Diffusion-weighted: 100 gradient orientations (900, 1600, 2500 s/mm^2 diffusion-weightings), 2 mm × 2 mm × 2 mm voxel size, 17 images without diffusion-weighting of which 5 in reverse phase-encoding direction. We performed correction for subject-motion [13], eddy current induced distortions [14], and echo-planar imaging distortions [15] with FMRIB Software Tools (FSL) [16]. Anisotropy tensors were calculated with constrained [17] weighted [18] and iterated (2 iterations) least squares [19] with MRtrix3 software package [20].

Transcranial magnetic stimulation

TMS was performed using a monophasic Magstim 200^2 stimulator (Magstim Company, UK) with a figure-of-eight coil (D70 Alpha Flat Coil, P/N 9925-00, Magstim Company, UK). A switch (Sälzer Electric GmbH, Rochlitz, Germany) installed in the coil cable to reverse the current direction without moving the coil. The coil position was tracked with the Visor2 TMS neuronavigation system (ANT Neuro, Enschede, the Netherlands) and verified with 3D scanning (Artec Leo, Artec 3D, Luxembourg) for accurate localization [21].

The participants sat on a reclining chair with hands on a pillow on their lap and head supported with a neck rest. The TMS coil was secured over the scalp with a mechanical holder. Participants were instructed to contract five hand and arm muscles (APB, FDI, ADM, ECU, and FCU) by applying consistent pressure by grasping a 10 cm diameter cork ball while monitoring their EMG activation displayed on a screen in front of them. They were instructed to maintain the amplitude of the EMG signal at approximately 200 μV peak to peak.

TMS pulses were delivered over the left cerebral hemisphere at 11 predetermined targets. Nine targets formed a 3 × 3 grid (4 cm × 4 cm), centred approximately over $[-41, -7, 63]$ in MNI coordinates. The coil direction was selected by measuring the motor threshold (MT) at the grid centre and adjusting the coil in 30° increments until the lowest threshold was found. The last two targets were at the grid centre with coil directions 30° clockwise and counterclockwise from the original direction (Fig. 1D). At each target, 10 pulses with a 2 s interstimulus interval (ISI) were delivered at increasing intensities (increment of 3% points) starting from 16% of the maximum stimulator output (MSO), up to a limit of 61%. The procedure was repeated using AP-TMS (starting at 17%, limit 62%).

Recording and analysis of motor evoked potentials

Motor evoked potential (MEPs) were recorded with NeurOne EMG system (NeurOne, MEGA Electronics Ltd, Finland) and disposable Ag/AgCl surface electrodes placed on APB, FDI, ADM, ECU, and FCU in a belly-tendon montage. EMG signals were sampled at 5 kHz and high-pass filtered with a 16 Hz cutoff frequency. In total, 106100 MEP signals were recorded.

The active motor threshold (AMT) and MEP latency were determined automatically using MEPICA.m (code and sample data available at: https://doi.org/10.5281/zenodo.12634513) with default settings. Briefly, the MEP signals (Fig. 1A) were decomposed into components representing different features of MEPs or baseline EMG activity (Fig. 1B) using reconstruction independent component analysis (ICA). ICA was applied separately for AP- and PA-TMS data to ensure that the MEP components of PA- and AP-TMS were not forced to be orthogonal. For each component, the MEP signals were classified into activations or non-activations by calculating whether the signal included the component in question. The AMT was defined as the intensity where the estimated activation probability exceeded 50% (Fig. 1C). This process was repeated for each MEP component, resulting in multiple AMT values corresponding to different coil locations and MEP components (Fig. 1D,E). Among all nine participants and five muscles, 602 AMTs were identified for PA-TMS and 370 for AP-TMS (Supplementary Figure 4).

Modelling of induced electric fields

The magnetic coil was modelled based on external dimensions obtained using a 3D scanner and measured electric fields in a spherical geometry [22] (Supplementary Figure 1). For each coil location, the induced electric field (Fig. 1F) was calculated in a participant-specific MRI-based head model with the finite-element method with first-order 1 mm × 1 mm×1 mm cubical elements using a geometric multigrid solver [23] (VGM-FEM, code and sample head model available at: https://version.aalto.fi/gitlab/ilaakso/vgm-fem). The head models were generated from the MRI using a segmentation pipeline [24] that used FreeSurfer (version 7.1.1) [25–27] for brain reconstruction. The tissue conductivity values used for the calculations were (unit: S/m) [9]: grey matter 0.215, white matter 0.142, CSF 1.79, dura mater 0.18, blood 0.7, skull spongiosa 0.034, skull compacta 0.009, scalp 0.43, muscle 0.18, fat 0.15, and eye 1.6. Anistropic conductivity of the white matter was obtained from diffusion tensor imaging (DTI) using the volume normalization technique [28,29].

Location-threshold-direction model of the activation site

The localization of the activation site was based on a model where the measured response originates from the activation of a single location $\mathbf{r}$ in the brain [12]. The location is activated if and only if the induced electric field in a preferred direction ($\mathbf{d}$) exceeds a threshold electric field (E_{thr}). This simple model is valid for neuroelectric excitation modes where the excitation is related to the strength of the

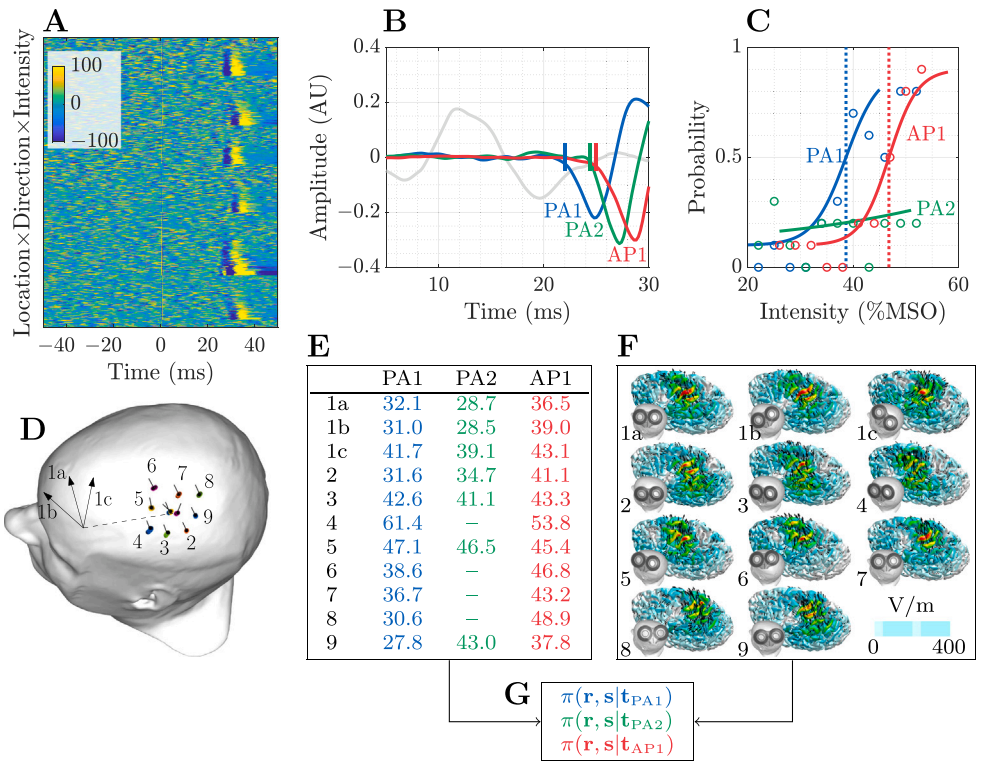

	PA1	PA2	AP1
1a	32.1	28.7	36.5
1b	31.0	28.5	39.0
1c	41.7	39.1	43.1
2	31.6	34.7	41.1
3	42.6	41.1	43.3
4	61.4	–	53.8
5	47.1	46.5	45.4
6	38.6	–	46.8
7	36.7	–	43.2
8	30.6	–	48.9
9	27.8	43.0	37.8

Fig. 1. Overview of the analysis process. **A.** Examples of MEP signals measured (unit: μV) in the active ADM muscle for multiple coil locations using both PA- and AP-TMS, multiple stimulation intensities, and ten signals per intensity. The magnetic stimulus was applied at 0 ms. **B.** Several features of the MEP signals were extracted using independent component analysis. Four illustrative MEP components are visualized: two components corresponding to PA-TMS (PA1 and PA2), one to AP-TMS (AP1), and one to baseline activity (grey curve). The MEP latency (vertical bars) was determined from the onset of each component. **C.** For each condition, the probability of evoking each MEP component was determined as a function of stimulation intensity. Logistic regression (curves) was used to determine the threshold intensity (dotted vertical lines) where the probability for evoking each component exceeded 50%. In the visualized example, no threshold was determinable for the PA2 component. **D.** Each participant was stimulated using both PA- and AP-TMS at nine coil locations with 3 coil orientations at the centre location (1a, 1b, and 1c). **E.** The analysis visualized in C was repeated to obtain a map of the thresholds for evoking each MEP component for each coil location. This analysis was repeated for APB, FDI, ADM (listed in the table as %MSO), ECU, and FCU muscles. **F.** The induced electric field corresponding to each coil location was calculated using a participant-specific MRI-based model. Electric field strengths calculated at the MSO are shown. **G.** The threshold data (E) and electric field data (F) were used as an input for a probabilistic model to produce a posterior probability density of the activation site ($\mathbf{r}$) and preferred activation direction and electric field threshold ($\mathbf{s}$) for each MEP component.

electric field instead of its gradient, *e.g.*, excitation at axonal bends or terminations in a near-uniform electric field [30,31]. Therefore, it is a useful approximation for modelling activations in both grey matter (terminations and bends) and white matter (bends). The model is also a good approximation for excitation due to field discontinuities at tissue interfaces, *e.g.*, between grey and white matter. However, this activation mode is unlikely [32]. In the following, the model is called the location-threshold-direction (LTD) model. We also combine the direction and threshold into a 'sensitivity vector' $\mathbf{s} = \mathbf{d}/E_{\text{thr}}$.

In the LTD model, given coil location $i = 1 \dots N$, the measured motor threshold t_i and induced electric field $\mathbf{E}_i$ at maximum stimulator output (MSO) are related by

$$t_i = \frac{1}{\mathbf{s} \cdot \mathbf{E}_i(\mathbf{r})} n, \tag{1}$$

where n is the noise term, chosen to be normally distributed with mean 1 and standard deviation $\frac{1}{20}$. Given the motor thresholds measured at multiple coil locations $\mathbf{t} = [t_1 \dots t_N]$ (Fig. 1E) and the corresponding electric field data (Fig. 1F), we solve a probabilistic inverse problem to determine the posterior distribution $\pi(\mathbf{s}, \mathbf{r}|\mathbf{t})$ for $\mathbf{r}$ and $\mathbf{s}$ [12] (LTDTMS.jl, available at: https://doi.org/10.5281/zenodo.10390898). Qualitatively, the choice of the location $\mathbf{r}$ and sensitivity vector $\mathbf{s}$ determines how well the model (1) explains the measured data. Therefore, $\mathbf{r}$ and $\mathbf{s}$ that could have plausibly generated the measured motor threshold data $\mathbf{t}$ are more probable than $\mathbf{r}$ and $\mathbf{s}$ for which $\mathbf{t}$ is unlikely (Supplementary Figure 2). It is important to note that the posterior probability is conditioned not only on the choice of the activation model (1) but also on the methods and modelling assumptions that were used for this study, described in the preceding subsections. To estimate the impact of the assumptions on the results, we performed a sensitivity analysis, varying some of the modelling parameters (Supplementary Table 2).

The following prior information was used for the LTD model. The prior of $\mathbf{s}$ was given by $|\mathbf{s}| < \frac{1}{E_{\text{thr,prior}}}$, where $E_{\text{thr,prior}} = 35$ V/m is the prior threshold electric field, below which no activation is believed to occur. The prior knowledge about $\mathbf{r}$ was that it needed to be in the brain tissue at < 30 mm distance from MNI coordinates $[-40.7, -15.7, 59.7]$ [33] and that $1.2 t_i |\mathbf{E}_i(\mathbf{r})| > E_{\text{thr,prior}}$ for each i.

To screen out cases where the data did not substantially support the LTD model, we calculated the Bayes factor of the LTD model against a reference model in which the thresholds were lognormally distributed and only included the cases where the Bayes factor was 3 or greater in the analysis (Supplementary Figure 4). After this screening, there were 50 localizations for PA-TMS and 20 localizations for AP-TMS (Supplementary Figure 4). The localization precision depended on the number of thresholds/coil locations used as the input data, such that a larger amount of data led to a more precise localization (Supplementary Figure 5).

Modelling of white matter tracts and axons

A white matter mask was obtained from corrected diffusion weighted (DW) images by using unsupervised 3-tissue response function estimation [20,34]. Fibre orientation distribution in the white matter was obtained via multi-shell constrained spherical deconvolution and normalization [20,35,36]. Finally, we generated 1000 tracts

having at least 0.5 mm radius of curvature and 5 mm length using parallel transport tractography (Trekker, [37,38]). The tracts were seeded from Brodmann areas Figs. 4p and 4a, based on the approximate cytoarchitectonic map produced using Freesurfer [39].

Models of ten nerve fibres (10 μm diameter, an order of magnitude estimate) were placed along each tract. The internodal distance of each fibre was 1 mm, and the Ranvier node locations were shifted in steps of 0.1 mm to produce ten axons with differing node locations. The cell membrane model was based on voltage-clamp measurements of a rabbit peripheral myelinated axon [40] and the nerve fibre model parameters were the same as those described previously [41,42] (sample implementation available at https://doi.org/10.5281/zenodo.12652749). Because cell bodies or synaptic terminals were not included, the axons were terminated with Dirichlet boundary conditions at both ends, ensuring that no spurious excitation could occur at the empty endings. No effort was made to tune the model parameters to better match those of the human central nervous system axons. The calculated electric fields (Fig. 1F) with the measured waveform (Supplementary Figure 1D) were used to excite the axon models, and the threshold for activating each tract was defined as the lowest stimulus intensity that triggered an action potential in all ten axons along the tract, searched using a binary search. The activation site of the tract was the mean over the ten locations where the action potentials were first initiated at the threshold intensity.

Statistical analysis

The LTD model produced a posterior distribution $\pi(\mathbf{s}, \mathbf{r}|\mathbf{t})$ for each unique combination of participant, muscle, MEP component, and current direction. Each such combination is called a *case* in the following.

The approach to analyse and visualize the results was to calculate marginal distributions from $\pi(\mathbf{s}, \mathbf{r}|\mathbf{t})$. For example, we could calculate the probability that the activation site is within the white matter by calculating the integral

$$P_{\mathrm{WM}} = \int_{\mathrm{WM}} \int \pi(\mathbf{s}, \mathbf{r}|\mathbf{t}) d\mathbf{s} d\mathbf{r}, \tag{2}$$

where the outer integral is over the entire white matter and the inner integral is over the entire threshold-direction space.

To investigate the probability data in the MNI space, we made a coordinate transform from the individual MRI space to the ICBM 2009a asymmetric template [43,44] using FreeSurfer (Supplementary Figure 3). The data in the MNI space was further transformed to depth, lateral–medial (LM), anterior–posterior (AP), coordinate system, where the depth axis was out of the brain, AP axis was at an angle of 45° to the midline being approximately perpendicular to the central sulcus, and LM axis was perpendicular to both depth and AP axes. The origin of this coordinate system was at $[-41, -21, 59]$ mm.

To visualize the posterior distributions, we used the `ksdensity` function of MATLAB to calculate 1D and 2D kernel density estimates of the posterior probability. When reporting average data over multiple cases, we calculated the probability density function of the average. Differences between cases were reported by constructing the probability density function of the difference. Possible dependencies between cases were not considered in the calculation of the probability densities of the averages or differences. To report uncertainty, highest posterior density volumes, areas and intervals were used.

Additionally, whenever relevant, we reported 95% confidence intervals (CI), Student's t-tests, Mann–Whitney *U*-tests, and linear mixed effects models. MATLAB was used for these analyses.

Results

MEP latency difference between PA- and AP-TMS

The MEP component latency of all cases are illustrated in Fig. 2A. When compared with the PA-TMS MEP component with the shortest latency, the latency of AP-TMS was on average 2.1 ms longer (SD: 1.4 ms, median: 2.2 ms, 95% CI: 1.2–3.0 ms, interquartile range (IQR): 1.1–3.2 ms, Fig. 2B). There was no evidence of the dependence of PA–AP latency difference on the muscle (Mann–Whitney U tests, all pairwise comparisons $p \geq 0.057$).

For PA-TMS cases with multiple MEP components, the latency difference of the later components compared with the component with the shortest latency was on average 2.3 ms (SD: 1.4 ms, median: 2.4 ms, 95% CI: 1.2–2.8 ms, IQR: 1.7–2.7 ms, Fig. 2C).

The AMTs were on average $38.4 \pm 8.5\%$ MSO for PA-TMS (Supplementary Figure 6C) and $43.2 \pm 8.1\%$ MSO for AP-TMS (Supplementary Figure 6B). The PA-TMS AMTs were significantly lower in all muscles but ECU (Supplementary Figure 6A).

Both PA- and AP-TMS are more likely to activate structures in white matter, with AP-TMS activations deeper and more posterior

We calculated the probabilities of the activation sites being in specific cortical areas obtained from FreeSurfer parcellation [39] or in the white matter under the pre- and postcentral gyri (Fig. 3A). On average, the activation site of PA-TMS was most likely in the white matter under the precentral gyrus (Fig. 3A), while the AP-TMS activation site was more likely to be located in the white matter of both the pre- and postcentral gyri. Activations in the cortical grey matter were less probable than those in white matter, with PA-TMS more likely to activate precentral areas (BA4a, BA4p, and BA6) and AP-TMS postcentral areas (BA3b, BA2, and BA1) (Fig. 3A).

The ratio of precentral and postcentral activation probabilities (odds) was separately investigated for each case (Fig. 3B). Substantial evidence, defined as three-fold odds, existed for 44/70 cases in favour of precentral activation and 17/70 in favour of postcentral activation (Fig. 3B). Nine cases had insufficient evidence to distinguish between pre- and postcentral activation (grey shaded area in Fig. 3B). On average, PA-TMS was 3900 times (geometric mean, 95% CI: 260–60000) more likely to activate the grey or white matter of the precentral gyrus than those of the postcentral gyrus. In contrast, AP-TMS showed no significant preference on average, with the odds slightly favouring postcentral activation (precentral activation 0.64 times as likely as postcentral activation, 95% CI: 0.05–8.9). There were five atypical cases for PA-TMS, four from a single participant, where there was strong evidence of a postcentral activation site (odds > 10). These corresponded to cases where there was little to no MEP latency difference between PA- and AP-TMS (Supplementary Table 1).

White and grey matter activations could not be separated in 41/70 cases. In 29 cases with substantial evidence, the odds favoured white matter in 26 and grey matter in 3 cases. On average, both PA-TMS and AP-TMS were significantly more likely to activate structures in the white matter rather than those in grey matter (PA-TMS: 1.81, 95% CI: 1.31–2.52, and AP-TMS: 5.50, 95% CI: 2.57–11.8) (Fig. 3C).

When transformed into the depth, LM, AP coordinate system, differences in mean coordinates between PA-TMS and AP-TMS were observed: AP-TMS activation sites were deeper (mean difference: 5.4 mm, 95% HPDI (highest posterior density interval): $[3.0, 7.9]$ mm), more lateral (mean difference: 3.4 mm, 95% HPDI: $[1.8, 5.1]$ mm), and more posterior (mean difference: 8.4 mm, 95% HPDI: $[6.2, 10.6]$ mm) (Fig. 3D–F).

Finally, the marginal distributions of the electric field threshold (E_{thr}) showed a small difference between PA- and AP-TMS (mean difference: 0.3 V/m, 95% HPDI: $[-7.0, 7.4]$ V/m) (Fig. 3G), which indicated that the neural structures activated by both PA- and AP-TMS were similarly sensitive to induced electric fields.

A sensitivity analysis of the results to model parameters was performed in four cases, showing minor effects of element size and conductivity values (Supplementary Table 2). For example, changing the white matter conductivity to 0.4 S/m led to up to 30% relative differences in the induced electric field, but the effects on the estimated activation probabilities were marginal (Supplementary Table 2). Changing the

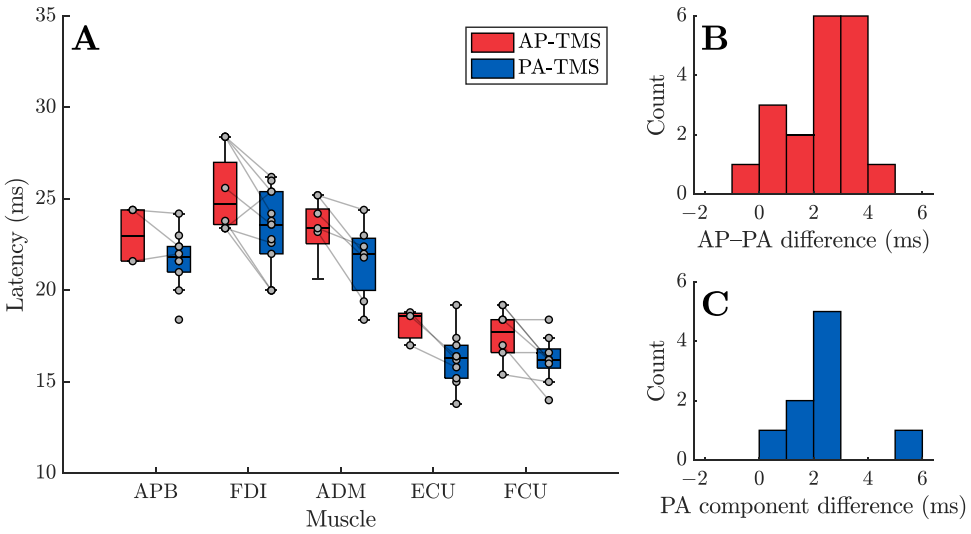

Fig. 2. The effect of muscle and current direction on the MEP component latency. **A.** Boxplot visualization of the MEP latencies for each muscle. Graphs represent the minimum, maximum, median, first quartile and third quartile in the data set. PA (blue) and AP (red) directed stimulations are separated for each muscle. Grey lines connect the data from the same participant between the coil directions. **B.** Histogram of the latency difference between PA- and AP-TMS, calculated using the earliest MEP component of PA-TMS as the reference. **C.** Latency difference between the earliest MEP component and other MEP components for PA-TMS. (For interpretation of the references to colour in this figure legend, the reader is referred to the web version of this article.)

activation model (1) such that only grey or white matter was excitable could greatly decrease the model plausibility in cases with large odds in favour of either matter over the other (Supplementary Table 2D). Over all 70 cases, these alternative activation models were never supported substantially over the default model (all Bayes factors < 2.4), but there were 13 cases where there was substantial evidence against (Bayes factor $< 1/3$) the alternative models (11 against grey matter only model, and 2 against white matter only model).

Small differences between muscle activation sites

The average activation sites of PA-TMS were located roughly at the centre of the hand knob (Fig. 4A), with small differences between the muscles. On average, ADM was the most medial and APB the most lateral. From the most medial to the most lateral, the mean differences (95% HPDI) in the lateral coordinate compared to ADM were: FCU: 3.4 [0.3, 6.5] mm, ECU: 4.1 [0.5, 7.6] mm, FDI: 5.2 [2.2, 8.2] mm, and APB: 6.2 [3.0, 9.4] mm. As also indicated earlier (Fig. 3B), the activation sites of AP-TMS were on average located under the postcentral gyrus (Fig. 4A). However, due to relatively few data, it could not be determined whether the AP-TMS activation sites followed a specific somatotopic pattern.

The preferred direction for PA-TMS activations (Fig. 4B) was close to 45° angle compared to the midsagittal line for FDI, APB, ECU, and FCU (mean differences to 45°: −8° to 6°). In the ADM, the direction was closer to the midsagittal line, 25° (95% HPDI: [12°, 38°]). Over all muscles, the average preferred direction was 41° (95% HPDI: [36°, 46°]). These findings support the commonly-used rule that the induced current direction should be approximately 45° to the midline for optimal stimulation. Furthermore, the more anterior optimal direction for ADM may reflect the more medial location of the activation site, where the direction of the central sulcus is more perpendicular to the midsagittal line (Fig. 4A).

For AP-TMS, the overall preferred direction was at 50° (95% HPDI: [41°, 59°]) angle to the negative midsagittal line (Fig. 4B). However, the data was insufficient to draw conclusions on muscle-specific differences in the optimal directions.

Stimulation of white matter tracts is a possible explanation for the activation sites and PA-AP latency differences

A possible explanation for activation site locations in grey matter is the activation of axon terminals, each of which follows a relationship similar to (1) [45]. However, this explanation is not valid for white matter activations, which were on average estimated to be more probable than grey matter activations. The activation site locations and directions in white matter could instead be explicable by direct activation of large myelinated axons in white matter tracts, as previously hypothesized [46].

To explore which white matter tracts are possibly activated, we generated 1000 tracts that started from M1 (Fig. 5A–C). Placing computational axon models along each tract and using the induced electric field data, we estimated the threshold intensity required for the activation of the tract for each coil location. We then calculated the coefficient of determination (R^2) between the estimated and measured thresholds, assuming direct proportionality. Each tract received an R^2 value, indicating the goodness-of-fit between the computationally estimated and measured motor thresholds. This analysis was repeated for all cases, also including those where the odds favoured grey matter activation. Fig. 5A–C illustrates the tracts with $R^2 > 0.8$, which constitute 3.4% of all simulated tracts, with the insets showing a close-up view with the ten best-fitting tracts highlighted. Over all subjects, the largest R^2 values ranged from 0.61 to 1.00 (median: 0.93, IQR: [0.89, 0.96]).

Next, we investigated whether the tracts with large R^2 were in the vicinity of the activation site found using the LTD method by finding the tracts whose trajectory touched the 95% highest posterior density volume (HPDV). The largest R^2 values of the touching tracts ranged from 0.61 to 1.00 (median: 0.92, IQR: [0.89, 0.96]) (Fig. 5D). Not all touching tracts had a large R^2 value, *e.g.*, 14% having $R^2 > 0.8$ (Supplementary Figure 7). The difference in the largest R^2 among the touching tracts compared to the maximum of all tracts was small (median: 0, IQR: [0, 0], range: −0.11 to 0), indicating that the best-fitting tracts also tended to touch the 95% HPDV. Thus, activation site locations found using the LTD method were potentially explicable by the activation of myelinated axons in white matter tracts. The sites of action potential initiation were typically at axonal bends in the precentral gyrus, postcentral gyrus, or deep in the U-fibres connecting the two gyri (insets of Fig. 5A–C and Supplementary Figure 9).

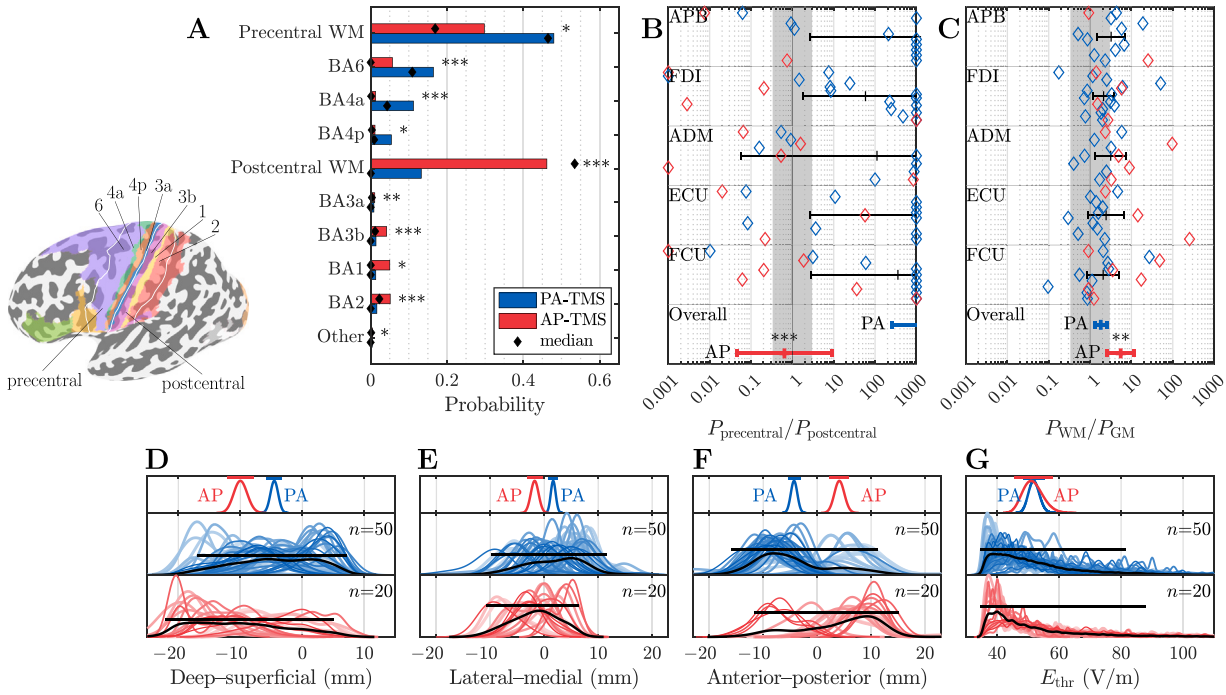

Fig. 3. Differences of the activation characteristics between PA- and AP-TMS. **A.** Mean (bars) and median (diamonds) probability of the activation site being in each Brodmann area (BA) or white matter (WM) under the precentral or postcentral gyri. Asterisks indicate p-values of the comparison between PA- and AP-TMS from Mann–Whitney *U* tests. **B.** Odds of the activation site being in precentral versus postcentral gyrus in all studied cases, grouped by the measured muscle. **C.** Odds of white matter versus grey matter activation. In B and C, blue and red markers indicate PA-TMS and AP-TMS, respectively. Cases where the odds were less than 0.001 or greater than 1000 are shown at the edge of the visualization area. Shading indicates the area between 1/3 and 3. Error bars are the median values and their 95% CIs obtained from fitted lognormal distributions. Asterisks indicate the *p*-value of the comparison between PA- and AP-TMS using unpaired Student's t-tests of log-transformed data. **D–G.** Marginal distributions of the depth, lateral–medial and anterior–posterior coordinates, and the threshold electric field for PA- and AP-TMS. The top panels show the probability density function of the averages for PA- and AP-TMS and the bottom panels show the individual probability density functions, along with the average probability density function (black). Horizontal bars indicate the 95% HPDI. (*: $p < 0.05$, **: $p < 0.01$, ***: $p < 0.001$). (For interpretation of the references to colour in this figure legend, the reader is referred to the web version of this article.)

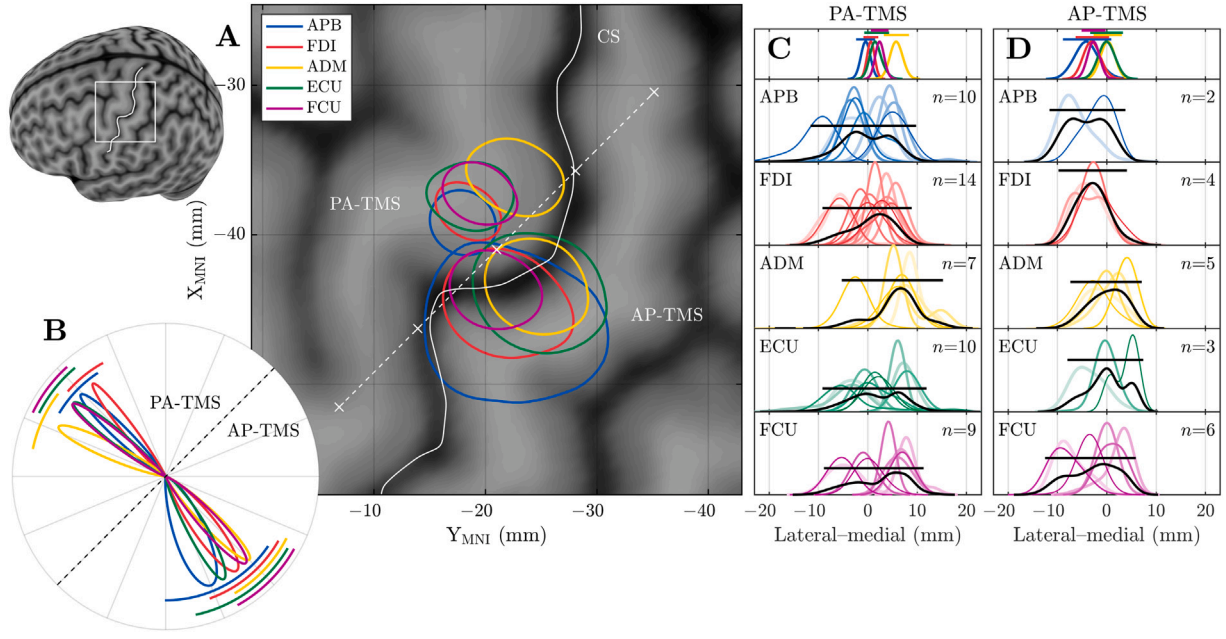

Fig. 4. Muscle activation sites of PA- and AP-TMS registered to the MNI brain. **A.** 95% highest posterior density bounds of the average activation site location for each muscle for PA- and AP-TMS. White curve illustrates the course of the central sulcus (CS). The dashed line indicates the direction with an angle of 45° to the midline, along which the lateral coordinate was calculated. **B.** Polar plot of the marginal distributions of the average preferred activation direction (average over all cases). Arcs are the 95% HPDIs of the preferred direction of activation. **C** and **D.** Marginal distributions of the lateral coordinate for PA- and AP-TMS. The top panel shows the probability density function of the averages for each muscle and the bottom panels show the individual probability density functions, along with the average probability density function (black). Horizontal bars indicate the 95% HPDI.

We further explored whether the MEP latency was related to the activation site locations. For each tract, we calculated the along-tract distance from the sites where the action potentials were triggered to the origin of the tract in M1. For each case, we chose the five tracts with the largest R^2 that touched the 95% HPDV and calculated the median of the distance over all sites. The results are shown in Fig. 5E. PA-TMS triggered action potentials at sites that were typically closer than 10 mm to M1 (median: 5 mm, IQR: $[4, 12]$ mm), corresponding to bends directly under the cortex (Supplementary Figure 9A), whereas AP-TMS action potentials were triggered at approximately 25 mm more distant locations (median: 30 mm, IQR: $[19, 38]$ mm). The difference was statistically significant (Mann–Whitney U test, $z = -5.4927$, $p = 1 \times 10^{-8}$), and could potentially explain the latency difference between PA- and AP-TMS. For comparison, the average length of the tracts from M1 to the crown of the postcentral gyrus (BA1) was 46 ± 12 mm (inter-individual variation in the mean: 43–50 mm), *i.e.*, if AP-TMS were to activate these tracts, the activation site would be in white matter of the postcentral gyrus at approximately 15 mm depth from the crown.

For the five best-fitting tracts described above, the minimum calculated activation thresholds were at median 2.0 times higher (IQR: 1.6–2.7) than the measured AMT (Supplementary Figure 8). The difference between the median values was not statistically significant between PA- and AP-TMS (Mann–Whitney U test, $z = 1.7616$, $p = 0.08$). A difference compared with measurements is expected as we made no efforts to tune the axon diameter or the cell membrane parameters, which have a large effect on the threshold [42].

If the PA-AP latency difference is due to a longer distance to M1, the conduction velocity along the tract can be estimated. For this purpose, we fitted a linear mixed effects model to the data using Akaike information criterion (AIC) for model selection. The candidate models had each combination of muscle, distance, and direction (PA or AP) and their interactions as fixed effects and subject-specific intercepts as random effects. The model that minimized the AIC (adjusted $R^2 = 0.89$) was the one with muscle and distance as the sole fixed effects (Fig. 5F). The estimated conduction velocity was 19 m/s (95% CI: $[12, 38]$ m/s), which is a typical value for a large myelinated axon, but much slower than that of corticospinal tract axons (50–70 m/s, [47]).

Discussion

The activation sites of PA- and AP-TMS were estimated using a probabilistic model that was fitted to AMT measurements. The model indicated that PA- and AP-TMS typically activated different locations in the brain, with AP-TMS activations deeper, more lateral, and more posterior. Unexpectedly, the model also indicated that both PA- and AP-TMS were more likely to be in white rather than grey matter, which was more pronounced for AP-TMS than for PA-TMS, differing from the conventional view that TMS primarily activates myelinated axons in the cortex [6]. Additionally, tractography-based biophysical axon modelling suggested that activation of bends of large myelinated axons in white matter tracts was a possible model for the activation site locations and might explain the observed latency differences between PA- and AP-TMS.

The probabilistic model localized AP-TMS activations in the white matter under the postcentral gyrus, but also under the precentral gyrus. A possible explanation for these activation locations was provided by tractography modelling, which suggested that the estimated locations were consistent with low-threshold sites of projection fibres from the primary somatosensory cortex (S1) to M1. While this result is based on modelling and should thus be taken with caution, there is earlier experimental evidence indicating that there are fast excitatory projection fibres from S1 to M1, which could be activated by AP-TMS. Previous experiments have shown short latency (1–6 ms) responses in M1 when S1 is directly stimulated, observed in both humans [48] and monkeys [49]. In monkeys, part of the projections from S1 send excitatory post-synaptic potentials monosynaptically to layer 5 PTNs with short latency (1.1–5.7 ms) [49]. Additionally, the probabilistic model indicated that the probability of premotor activations was negligibly small, and hence, our results do not support the previous hypotheses that AP-TMS would activate premotor areas based on neurone modelling [45] and functional connectivity measurements [50].

Unlike for AP-TMS, our model indicated that PA-TMS activated either white or grey matter in the precentral gyrus, although white matter activation was 1.8 times more likely than grey matter activation. The activation site locations were typically located in the anterior wall of the central sulcus, corresponding to the locations of axonal bends in white matter under the cortex. Activation of grey matter elements, *i.e.*, terminals of intracortical axons [45], immediately adjacent to these bends was another non mutually exclusive explanation for the activation location. Our data provides little information whether the activated axons belong to, *e.g.*, afferent cortico-cortical or thalamocortical projection fibres, or to PTNs. If the activated axons are afferent projections, our latency measurements suggest that the PA-AP latency difference, typically between 2–4 ms (Fig. 2B), could be explained by AP-TMS activating S1-M1 projections further from M1 and PA-TMS activating the same or other projections closer to M1, with the longer latency of AP-TMS responses due to a conduction velocity of approximately 20 m/s. Notably, there was little to no PA-AP latency difference in one participant where PA-TMS likely activated postcentral white matter (Supplementary Table 1).

The latter option that the activated axons could be those of PTNs, raises a major question, as experimental evidence from epidural spinal recordings suggests that low-intensity TMS presumably does not directly activate PTN axons [5]. We note that the lack of direct PTN activation is similarly puzzling for the hypothesis that TMS would predominantly activate axons in the cortex [6,45]. Why are large PTN axons not activated, even though peripheral nerve fibres can be readily activated with electric fields of similar or weaker strengths? For instance, the average threshold for sensation in the human forearm would be approximately 30 V/m for our TMS waveform (Supplementary Figure 1D), estimated from the measured strength-duration parameters [51]. Similar threshold estimates can be obtained from classical axon electrostimulation models [31,52]. Only hypothetical explanations can be provided: as PTN axons likely have long internodal distances, the bend could occur before the first Ranvier node, and thus, the axon would appear as relatively straight in terms of induced depolarization and thus difficult to activate with TMS (the axon initial segment is not easily excitable [53,54]); and/or cortico-cortical or intracortical axons, despite their presumably smaller diameter, could still be more excitable than PTN axons due to their geometric or biological properties, *e.g.*, bend angle, ion channel density, internode length, internodal axon diameter, and node diameter [55]. To better answer the question, further experiments and modelling are needed on the differences between TMS and transcranial electrical stimulation, which presumably activates PTNs directly [5].

Confirmation of the suggested activation locations of PA- and AP-TMS could be attempted experimentally in non-human primates, where the activity of single neurons can be measured simultaneously with the TMS pulse [56]. Indirect ways to test the validity of our model predictions in humans would be to use short-latency afferent inhibition (SAI) [57] or paired pulse protocols with differently directed currents [58,59] to see whether the SAI at different inter-stimulus intervals is compatible with a possible conduction delay between activation sites. Recently, it has also become possible to measure pulse-direction dependent EEG responses starting at 2 ms after the stimulus [60], which could be used to study how the evoked potentials spread to adjacent brain areas from the activation sites of PA- and AP-TMS.

Regardless of whether the hypothesis of TMS activating white matter is true, our tractography-based axon-activation model was capable of explaining experimental observations of the AMT and possibly the PA-AP latency difference. Therefore, it could be a useful computational

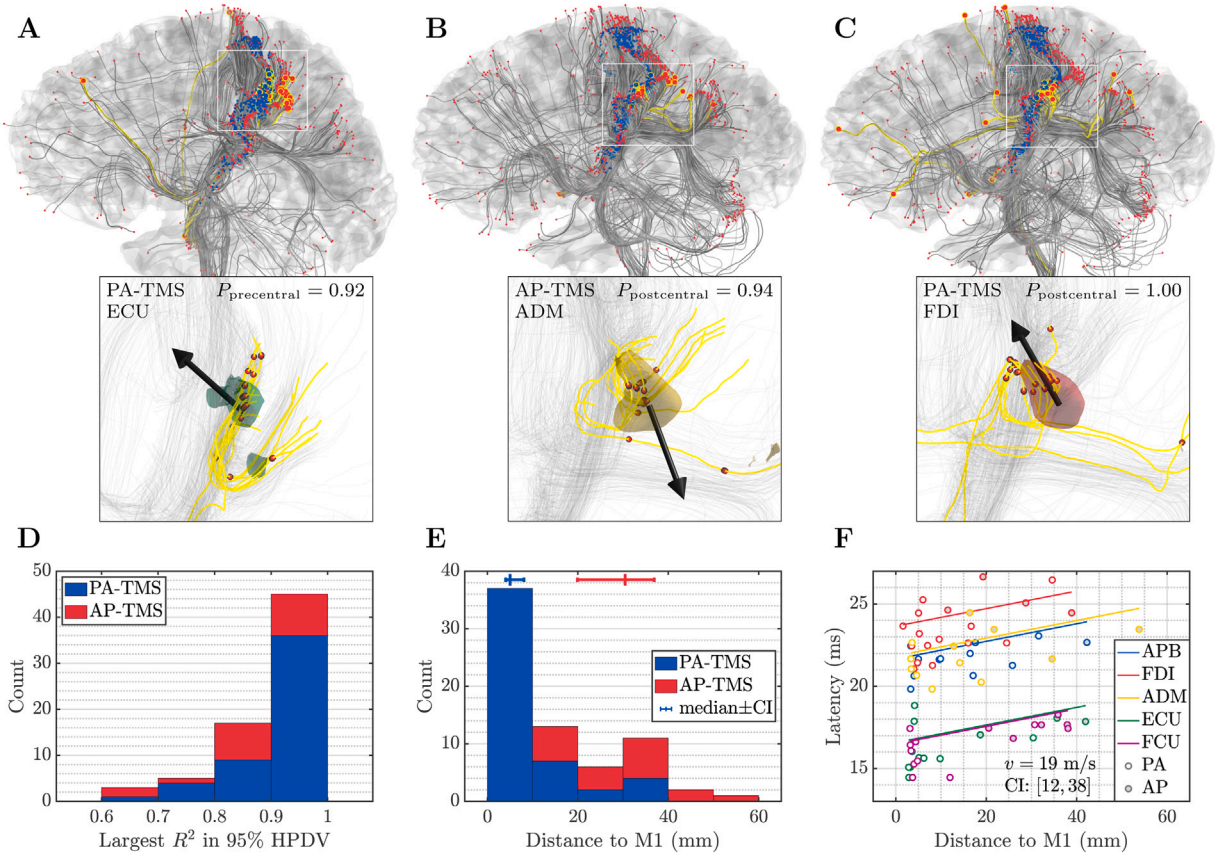

Fig. 5. Computational axon modelling of white matter tract activations. **A–C.** Visualization of neural tracts of three representative cases. The tracts were seeded in the primary motor cortex (blue markers) and ended in arbitrary areas (red markers). The tracts with R^2 value smaller than 0.8 are coloured in grey and the tracts with R^2 value higher than 0.8 are highlighted in yellow. Insets show close-up views of the 95% highest posterior density volume (HPDV) and the ten tracts with the largest R^2 values. Red markers indicate the sites where the action potentials are initiated with the lowest threshold for each coil location, and the black arrow (length: 15 mm) is the expected value of the preferred activation direction from the LTD model. **D.** The largest R^2 value among the tracts that touch the 95% HPDV. The stacked bar plot visualizes the number of tracts with the certain maximal R^2 value. **E.** Distance along the tract from the activation site to M1. The sites where action potentials were triggered were determined for the five tracts that have the largest R^2 and touch the 95% HPDV. The median distance along the tract to the origin was then calculated. **F.** Linear mixed effect regression between the distance from the estimated activation site to M1 and the measured MEP latency. The participant-specific random intercepts have been subtracted from the data points for visualization. The slope of the linear fit is the inverse of the conduction velocity. (For interpretation of the references to colour in this figure legend, the reader is referred to the web version of this article.)

tool for optimizing TMS protocols, as also suggested earlier [46]. For example, the approach can be used to optimally position the TMS coil to activate specific neural tracts individually in each participant or patient, which can be done offline prior to TMS based on diffusion MRI tractography information. Tractography data has already been demonstrated to predict the spread of direct cortical stimulation to other areas in measurements taken during epilepsy surgeries [61,62]. Any such tracts are potential targets for TMS and can be readily modelled, which may aid the development of new personalized TMS protocols, also in non-motor targets. However, the optimal choice of the axon model parameters should be investigated in future studies [42,63].

Additionally, our findings on muscle-specific activation sites showed only small differences on average, but ADM was more medial than APB/FDI, consistent with functional magnetic resonance imaging studies of finger use [64]. However, it should be noted that the obtained map of activation site locations may not correspond to the cortical organization, if activation occurred in axons in the white matter, whose exact destinations in the cortex are not clear. The failure to achieve differentiation between different muscles is not unexpected, as M1 has a distributed organization with overlapping muscle representations [65–67].

There are some important features and limitations to our methods. Firstly, while the experimental observations supported our probabilistic activation model, alternative models cannot be excluded, as the same observations can support multiple different models. Secondly, our probabilistic method does not identify all possible activations but instead produces a probability distribution for a single activation. TMS likely activated many axons at various locations, and only a few were found using our method. The identified activation sites may not necessarily be representative of the whole population of activation sites, especially if the likelihood of finding an activation site correlates with some the site's features, *e.g.*, being in white or grey matter. Thirdly, we chose to perform the measurements in active muscles because the AMT is a more direct measure of cortical activation than the resting motor threshold, as EMG responses in resting muscles are suppressed by the lowered excitability of spinal motoneurones [4]. The hand gesture (static grasp with locked wrist) was selected to ensure that all five muscles were active. However, it is possible that activations in M1 depend on the specific task being performed [48], which may affect the muscle activation sites. A limitation of our study is that relatively few AP-TMS activations could be localized, which was due to the smaller number of thresholds for AP-TMS. This limitation partly arose because we capped the stimulation intensity at 62% of the MSO, so all thresholds higher than this could not be obtained.

CRediT authorship contribution statement

Ilkka Laakso: Writing – original draft, Visualization, Supervision, Software, Methodology, Funding acquisition, Formal analysis, Data curation, Conceptualization. **Juhani Kataja:** Writing – review & editing, Software, Methodology, Investigation, Formal analysis, Data curation.

Noora Matilainen: Writing – review & editing, Visualization, Methodology, Investigation, Formal analysis. **Timo Roine:** Writing – review & editing, Methodology. **Thomas Tarnaud:** Writing – review & editing, Methodology. **Yoshikazu Ugawa:** Writing – review & editing.

Funding

This work was supported by Research Council of Finland [grant nos. 325326 and 362610].

Declaration of competing interest

The authors declare that they have no known competing financial interests or personal relationships that could have appeared to influence the work reported in this paper.

Supplementary data

Supplementary material related to this article can be found online at https://doi.org/10.1016/j.brs.2025.02.003.

References

[1] Day BL, Dressler D, de Noordhout AM, Marsden CD, Nakashima K, Rothwell JC, et al. Electric and magnetic stimulation of human motor cortex: surface EMG and single motor unit responses. J Physiol (Lond) 1989;412:449–73.
[2] Sakai K, Ugawa Y, Terao Y, Hanajima R, Furubayashi T, Kanazawa I. Preferential activation of different I waves by transcranial magnetic stimulation with a figure-of-eight-shaped coil. Exp Brain Res 1997;113(1):24–32.
[3] Patton HD, Amassian VE. Single and multiple-unit analysis of cortical stage of pyramidal tract activation. J Neurophysiol 1954;17(4):345–63.
[4] Di Lazzaro V, Restuccia D, Oliviero A, Profice P, Ferrara L, Insola A, et al. Effects of voluntary contraction on descending volleys evoked by transcranial stimulation in conscious humans. J Physiol (Lond) 1998;508(Pt 2):625–33.
[5] Di Lazzaro V, Rothwell JC. Corticospinal activity evoked and modulated by non-invasive stimulation of the intact human motor cortex. J Physiol (Lond) 2014;592(19):4115–28.
[6] Siebner HR, Funke K, Aberra AS, Antal A, Bestmann S, Chen R, et al. Transcranial magnetic stimulation of the brain: What is stimulated? – a consensus and critical position paper. Clin Neurophysiol 2022;140:59–97.
[7] Peterchev AV, Goetz SM, Westin GG, Luber B, Lisanby SH. Pulse width dependence of motor threshold and input–output curve characterized with controllable pulse parameter transcranial magnetic stimulation. Clin Neurophysiol 2013;124(7):1364–72.
[8] Bungert A, Antunes A, Espenhahn S, Thielscher A. Where does TMS stimulate the motor cortex? Combining electrophysiological measurements and realistic field estimates to reveal the affected cortex position. Cereb Cortex 2016;27(11):5083–94.
[9] Laakso I, Murakami T, Hirata A, Ugawa Y. Where and what TMS activates: experiments and modeling. Brain Stimul 2018;11:166–74.
[10] Weise K, Numssen O, Thielscher A, Hartwigsen G, Knösche TR. A novel approach to localize cortical TMS effects. Neuroimage 2020;209:116486.
[11] Numssen O, Zier AL, Thielscher A, Hartwigsen G, Knösche TR, Weise K. Efficient high-resolution TMS mapping of the human motor cortex by nonlinear regression. NeuroImage 2021;245:118654.
[12] Kataja J, Soldati M, Matilainen N, Laakso I. A probabilistic transcranial magnetic stimulation localization method. J Neural Eng 2021;18(4):0460f3.
[13] Leemans A, Jones DK. The b-matrix must be rotated when correcting for subject motion in dti data. Magn Reson Med 2009;61(6):1336–49.
[14] Andersson JL, Sotiropoulos SN. An integrated approach to correction for off-resonance effects and subject movement in diffusion mr imaging. NeuroImage 2016;125:1063–78.
[15] Andersson JL, Skare S, Ashburner J. How to correct susceptibility distortions in spin-echo echo-planar images: application to diffusion tensor imaging. NeuroImage 2003;20(2):870–88.
[16] Jenkinson M, Beckmann CF, Behrens TE, Woolrich MW, Smith SM. FSL. NeuroImage 2012;62(2):782–90.
[17] Morez J, Szczepankiewicz F, den Dekker AJ, Vanhevel F, Sijbers J, Jeurissen B. Optimal experimental design and estimation for q-space trajectory imaging. Hum Brain Ma 2022;44(4):1793–809.
[18] Basser P, Mattiello J, Lebihan D. Estimation of the effective self-diffusion tensor from the NMR spin echo. J Magn Reson Ser B. 1994;103(3):247–54.
[19] Veraart J, Sijbers J, Sunaert S, Leemans A, Jeurissen B. Weighted linear least squares estimation of diffusion MRI parameters: Strengths, limitations, and pitfalls. NeuroImage 2013;81:335–46.
[20] Tournier JD, Smith R, Raffelt D, Tabbara R, Dhollander T, Pietsch M, et al. Mrtrix3: A fast, flexible and open software framework for medical image processing and visualisation. NeuroImage 2019;202:116137.
[21] Matilainen N, Kataja J, Laakso I. Verification of neuronavigated TMS accuracy using structured-light 3D scans. Phys Med Biol 2024;69(8):085004.
[22] Nieminen JO, Koponen LM, Ilmoniemi RJ. Experimental characterization of the electric field distribution induced by TMS devices. Brain Stimul 2015;8(3):582–9.
[23] Laakso I, Hirata A. Fast multigrid-based computation of the induced electric field for transcranial magnetic stimulation. Phys Med Biol 2012;57(23):7753–65.
[24] Mikkonen M. Individualized computational modeling of transcranial direct current stimulation. (Doctoral Dissertations 5/2020), In: Aalto university publication series, 2020.
[25] Dale AM, Fischl B, Sereno MI. Cortical surface-based analysis. i. segmentation and surface reconstruction. Neuroimage 1999;9(2):179–94.
[26] Fischl B, Sereno MI, Dale AM. Cortical surface-based analysis. ii: Inflation, flattening, and a surface-based coordinate system. Neuroimage 1999;9(2):195–207.
[27] Fischl B, Sereno MI, Tootell RB, Dale AM. High-resolution intersubject averaging and a coordinate system for the cortical surface. Hum Brain Ma 1999;8(4):272–84.
[28] Güllmar D, Haueisen J, Reichenbach JR. Influence of anisotropic electrical conductivity in white matter tissue on the EEG/MEG forward and inverse solution, a high-resolution whole head simulation study. Neuroimage 2010;51(1):145–63.
[29] Kataja J, Nissi J, Roine T, Laakso I. Material coarsening strategy for structured meshless multigrid method for dosimetry in anisotropic human body models. IEEE Trans Electromagn Compat 2023;65(6):1–9.
[30] Maccabee PJ, Amassian VE, Eberle LP, Cracco RQ. Magnetic coil stimulation of straight and bent amphibian and mammalian peripheral nerve in vitro: locus of excitation. J Physiol (Lond) 1993;460:201–19.
[31] Reilly JP, Diamant AM. Electrostimulation: theory, applications, and computational model. first ed.. Norwood: Artech House; 2011.
[32] Salvador R, Silva S, Basser PJ, Miranda PC. Determining which mechanisms lead to activation in the motor cortex: a modeling study of transcranial magnetic stimulation using realistic stimulus waveforms and sulcal geometry. Clin Neurophysiol 2011;122(4):748–58.
[33] Diekhoff S, Uludağ K, Sparing R, Tittgemeyer M, Cavuşoğlu M, von Cramon DY, et al. Functional localization in the human brain: Gradient-echo, spin-echo, and arterial spin-labeling fMRI compared with neuronavigated TMS. Hum Brain Ma 2011;32(3):341–57.
[34] Dhollander T, Raffelt D, Connelly A. Unsupervised 3-tissue response function estimation from single-shell or multi-shell diffusion MR data without a co-registered T1 image. In: ISMRM workshop on breaking the barriers of diffusion MRI. vol. 5, Lisbon, Portugal; 2016.
[35] Jeurissen B, Tournier JD, Dhollander T, Connelly A, Sijbers J. Multi-tissue constrained spherical deconvolution for improved analysis of multi-shell diffusion MRI data. NeuroImage 2014;103:411–26.
[36] Raffelt D, Dhollander T, Tournier JD, Tabbara R, Smith R, Pierre E, et al. Bias field correction and intensity normalisation for quantitative analysis of apparent fibre density. In: Proc. ISMRM. 2017.
[37] Aydogan DB, Shi Y. Parallel transport tractography. IEEE Trans Med Imaging 2021;40(2):635–47.
[38] Aydogan DB, Shi Y. A novel fiber tracking algorithm using parallel transport frames. In: Proceedings of the 27th annual meeting of the international society of magnetic resonance in medicine. ISMRM, 2019.
[39] Fischl B, Rajendran N, Busa E, Augustinack J, Hinds O, Yeo BTT, et al. Cortical folding patterns and predicting cytoarchitecture. Cereb Cortex 2008;18(8):1973–80.
[40] Chiu SY, Ritchie JM, Rogart RB, Stagg D. A quantitative description of membrane currents in rabbit myelinated nerve. J Physiol (Lond) 1979;292:149–66.
[41] Basser PJ, Roth BJ. Stimulation of a myelinated nerve axon by electromagnetic induction. Med Biol Eng Comput 1991;29(3):261–8.
[42] Reilly JP. Survey of numerical electrostimulation models. Phys Med Biol 2016;61(12):4346–63.
[43] Fonov V, Evans A, McKinstry R, Almli C, Collins D. Unbiased nonlinear average age-appropriate brain templates from birth to adulthood. Neuroimage 2009;47(Supplement 1):S102.
[44] Fonov V, Evans AC, Botteron K, Almli CR, McKinstry RC, Collins DL, et al. Unbiased average age-appropriate atlases for pediatric studies. Neuroimage 2011;54(1):313–27.
[45] Aberra AS, Wang B, Grill WM, Peterchev AV. Simulation of transcranial magnetic stimulation in head model with morphologically-realistic cortical neurons. Brain Stimul 2020;13(1):175–89.
[46] Nummenmaa A, McNab JA, Savadjiev P, Okada Y, Hämäläinen MS, Wang R, et al. Targeting of white matter tracts with transcranial magnetic stimulation. Brain Stimul 2014;7(1):80–4.
[47] Boyd SG, Rothwell JC, Cowan JM, Webb PJ, Morley T, Asselman P, et al. A method of monitoring function in corticospinal pathways during scoliosis surgery with a note on motor conduction velocities. J Neurol Neurosurg Psychiatry 1986;49(3):251–7.

[48] Shelchkova ND, Downey JE, Greenspon CM, Okorokova EV, Sobinov AR, Verbaarschot C, et al. Microstimulation of human somatosensory cortex evokes task-dependent, spatially patterned responses in motor cortex. Nat Commun 2023;14(1).
[49] Ghosh S, Porter R. Corticocortical synaptic influences on morphologically identified pyramidal neurones in the motor cortex of the monkey. J Physiol (Lond) 1988;400(1):617–29.
[50] Volz LJ, Hamada M, Rothwell JC, Grefkes C. What makes the muscle twitch: Motor system connectivity and TMS-induced activity. Cereb Cortex 2015;25(9):2346–53.
[51] Havel W, Nyenhuis J, Bourl J, Foster K, Geddes L, Graber G, et al. Comparison of rectangular and damped sinusoidal db/dt waveforms in magnetic stimulation. IEEE Trans Magn 1997;33(5):4269–71.
[52] Reilly JP. Peripheral nerve stimulation by induced electric currents: Exposure to time-varying magnetic fields. Med Biol Eng Comput 1989;27(2):101–10.
[53] Nowak LG, Bullier J. Axons, but not cell bodies, are activated by electrical stimulation in cortical gray matter I. evidence from chronaxie measurements. Exp Brain Res 1998;118(4):477–88.
[54] Nowak LG, Bullier J. Axons, but not cell bodies, are activated by electrical stimulation in cortical gray matter II. evidence from selective inactivation of cell bodies and axon initial segments. Exp Brain Res 1998;118(4):489–500.
[55] Ford MC, Alexandrova O, Cossell L, Stange-Marten A, Sinclair J, Kopp-Scheinpflug C, et al. Tuning of ranvier node and internode properties in myelinated axons to adjust action potential timing. Nat Commun 2015;6(1).
[56] Mueller JK, Grigsby EM, Prevosto V, Petraglia FW, Rao H, Deng ZD, et al. Simultaneous transcranial magnetic stimulation and single-neuron recording in alert non-human primates. Nat Neurosci 2014;17(8):1130–6.
[57] Ni Z, Charab S, Gunraj C, Nelson AJ, Udupa K, Yeh IJ, et al. Transcranial magnetic stimulation in different current directions activates separate cortical circuits. J Neurophysiol 2011;105(2):749–56.
[58] Hanajima R, Ugawa Y, Terao Y, Sakai K, Furubayashi T, Machii K, et al. Paired-pulse magnetic stimulation of the human motor cortex: differences among I waves. J Physiol (Lond) 1998;509(2):607–18.
[59] Hanajima R, Ugawa Y, Terao Y, Enomoto H, Shiio Y, Mochizuki H, et al. Mechanisms of intracortical I-wave facilitation elicited with paired-pulse magnetic stimulation in humans. J Physiol (Lond) 2002;538(1):253–61.
[60] Beck MM, Christiansen L, Madsen MAJ, Jadidi AF, Vinding MC, Thielscher A, et al. Transcranial magnetic stimulation of primary motor cortex elicits an immediate transcranial evoked potential. Brain Stimul 2024.
[61] Silverstein BH, Asano E, Sugiura A, Sonoda M, Lee MH, Jeong JW. Dynamic tractography: Integrating cortico-cortical evoked potentials and diffusion imaging. NeuroImage 2020;215:116763.
[62] van Blooijs D, van den Boom MA, van der Aar JF, Huiskamp GM, Castegnaro G, Demuru M, et al. Developmental trajectory of transmission speed in the human brain. Nat Neurosci 2023;26(4):537–41.
[63] Tarnaud T, Joseph W, Martens L, Tanghe E. Dependence of excitability indices on membrane channel dynamics, myelin impedance, electrode location and stimulus waveforms in myelinated and unmyelinated fibre models. Med Biol Eng Comput 2018;56(9):1595–613.
[64] Huber L, Finn ES, Handwerker DA, Bönstrup M, Glen DR, Kashyap S, et al. Sub-millimeter fMRI reveals multiple topographical digit representations that form action maps in human motor cortex. NeuroImage 2020;208:116463.
[65] Ejaz N, Hamada M, Diedrichsen J. Hand use predicts the structure of representations in sensorimotor cortex. Nat Neurosci 2015;18(7):1034–40.
[66] Rathelot JA, Strick PL. Subdivisions of primary motor cortex based on cortico-motoneuronal cells. Proc Natl Acad Sci USA 2009;106(3):918–23.
[67] Gordon EM, Chauvin RJ, Van AN, Rajesh A, Nielsen A, Newbold DJ, et al. A somato-cognitive action network alternates with effector regions in motor cortex. Nature 2023;617(7960):351–9.